Optimal Green Energy Harvesting for Hybrid Photovoltaic-thermoelectric Generator System via Chaotic RIME Optimizer: a Techno-environmental Assessment

Jingbo Wang, Jianfeng Wen, Shaocong Wu, Bo Yang, Pingliang Zeng, and Lin Jiang

***Abstract*—This study develops a hybrid photovoltaic-thermoelectric generator (PV-TEG) system to reduce dependence on fossil fuels and promote sustainable energy generation. However, the inherent randomness of real-world operational environments introduces challenges such as partial shading conditions and uneven temperature distribution within PV and TEG modules. These factors can significantly degrade system performance and reduce energy conversion efficiency. To tackle these challenges, this paper proposes an advanced optimal power extraction strategy and develops a chaotic RIME (c-RIME) optimizer to achieve dynamic maximum power point tracking (MPPT) across varying operational scenarios. Compared with existing methods, this approach enhances the effectiveness and robustness of MPPT, particularly under complex working conditions. Furthermore, the study incorporates a comprehensive assessment framework that integrates both technical performance and sustainability considerations. A broader range of realistic operational scenarios are analyzed, with case studies utilizing on-site data from Hong Kong and Ningxia for technical and environmental evaluations. Simulation results reveal that the c-RIME-based MPPT technique can effectively enhance system energy output with smaller power fluctuations than existing methods. For instance, under startup testing conditions, the c-RIME optimizer achieves energy output increase by up to 126.67% compared to the arithmetic optimization algorithm.**

***Index Terms*—Photovoltaic-thermoelectric generator system, optimal energy harvesting, partial shading conditions, rime optimization algorithm, maximum power extraction technique.**

I. Introduction

There is broad consensus on the urgent need for global actions to combat climate change, with many nations pledging explicit carbon neutrality targets [1]. Achieving net-zero emissions by 2050 is essential for transforming economic, energy, and industrial systems, and for accelerating the transition to sustainable energy. In this context, the renewable energy sector must emphasize technological innovation, efficient resource utilization, and low-carbon development strategies [2]. Photovoltaic (PV) systems are extensively utilized owing to their abundant energy resources, zero-emission operations, and cost-effectiveness.

Nevertheless, PV systems also face notable limitations, such as low solar energy density and sensitivity to seasonal, locational, and climatic influences. During the process of photoelectric conversion, a significant share of the absorbed solar energy is lost as waste heat. Conventional silicon PV cells typically convert only 15%–18% of irradiance into electricity [3]. This thermal accumulation reduces the energy conversion efficiency of PV systems and module durability, with a 20 ℃ temperature increase potentially causing a 15% drop in power output [4]. Under hot summer conditions, the surface temperature of PV modules can exceed 66 ℃ [5]. Therefore, the recovery and utilization of this excess heat provide a promising solution to enhance energy efficiency while protecting PV modules from thermal degradation [6]. To this end, this study explores the integration of PV systems with thermoelectric generator (TEG) modules [7] to effectively harness waste heat, commonly referred to as a hybrid PV-TEG system [8]. TEGs, operating on the Seebeck effect [9], can convert

Received: December 30, 2024
Accepted: August 15, 2025
Published Online: November 1, 2025

Jingbo Wang, Jianfeng Wen, and Lin Jiang (corresponding author) are with the Department of Electrical Engineering and Electronics, University of Liverpool, Liverpool L69 3GJ, UK (e-mail: jingbo.wang@liverpool.ac.uk; j.wen7@liverpool.ac.uk; ljiang@liverpool.ac.uk).

Shaocong Wu is with the School of Electrical Engineering, Shandong University, Jinan 250061, China (e-mail: 798597909@qq.com).

Bo Yang is with the Faculty of Electric Power Engineering, Kunming University of Science and Technology, Kunming 650500, China (e-mail: yangbo_ac@outlook.com).

Pingliang Zeng is with the School of Automation, Hangzhou Dianzi University, Hangzhou 310018, China (e-mail: plz@hdu.edu.cn).

DOI: 10.23919/PCMP.2025.000004

temperature differences into electricity [10], positioning them as a viable solution for utilizing residual heat. To date, several hybrid PV-TEG designs have been developed [11], showing overall power output improvements ranging from 3% to 16% compared to standalone PV systems. These hybrid systems enhance both energy generation and the operational reliability of PV modules, benefiting from the passive cooling effects of TEG components [12]. In such a configuration, TEG modules are installed directly beneath PV panels [13]. However, real-world environmental conditions are inherently dynamic and continuously changing [14]. Partial shading conditions (PSCs), caused by obstructions like trees, buildings, or clouds, frequently impact PV arrays [15]. These shading effects result in localized increases in PV cell temperatures, a phenomenon known as the hotspot effect. This excessive heat buildup not only lowers energy conversion efficiency but can also cause irreversible damage to the structural integrity of PV modules [16]. Meanwhile, such hybrid configurations inevitably cause non-uniform thermal distribution (NTD) [17] among TEGs, further distorting the overall output characteristics of the system with more local maximum power points (LMPPs) [18]. Under these circumstances, a robust and accurate maximum power point tracking (MPPT) technique that can dynamically locate the global maximum power point (GMPP) is both essential and challenging, particularly under complex environments characterized by fluctuating irradiance and temperature [19].

Various MPPT strategies have been designed for standalone PV/TEG systems and integrated PV-TEG configurations [20], which can generally be categorized into conventional methods and intelligent algorithms. Conventional approaches, such as perturb and observe (P&O) [21] and incremental conductance (INC) [22], are primarily designed to track a single LMMP. They often fail to overcome the complexities associated with multiple LMPPs, leading to reduced energy harvesting efficiency. To address these limitations, more advanced methods are required. Model-free meta-heuristic algorithms excel at simplifying solution complexity and enhancing self-adaptive capabilities, making them well-suited for complex tracking scenarios. For instance, horse herd optimization (HHO) [23] and improved moth flame optimization [24] have been specifically proposed to optimize power extraction for PV and TEG systems. Reference [25] integrates the grey wolf optimizer (GWO) with cuckoo search (CS) to enhance convergence stability and speed, thereby improving overall system performance. A detailed review in [26] examines the utilization, advantages, and limitations of current MPPT algorithms for PV systems. Furthermore, dynamic surrogate model-based techniques are introduced for optimizing TEG outputs [27].

However, research specifically targeting hybrid PV-TEG MPPT control remains relatively limited, with only a few representative studies available. Reference [28] develops an arithmetic optimization algorithm (AOA) based MPPT control strategy for hybrid PV-TEG systems, which is validated under non-uniform temperature distribution. However, it suffers from limited exploration ability in complex search spaces. In addition, the atomic orbital search (AOS) optimization applied in [29] to ensure stable power extraction shows performance degradation in scenarios with multiple local optima, and its convergence slows during the final optimization stages. Notably, both AOA and AOS studies include only a narrow set of benchmark algorithms, which limits the generalizability and persuasiveness of their results, especially under diverse and realistic operating scenarios. Meanwhile, work in [30] utilizes salp swarm algorithm (SSA) to improve MPPT performance under PSCs, showing superior power output. Nevertheless, it exhibits slightly delayed stabilization and lower energy capture efficiency under highly stochastic cases. In general, research on this problem remains in its early stages and requires more comprehensive investigation. Although existing metaheuristic methods have advanced MPPT control in hybrid PV-TEG systems, challenges persist in achieving fast convergence, high stability, and robust adaptability under varied and dynamic environmental conditions.

To build upon previous efforts, three critical issues must be further explored. First, enhancements are needed to enhance power extraction under diverse PSCs. More effective MPPT strategies can alleviate the adverse impacts of PSCs, thereby boosting system reliability and economic viability. Second, most existing MPPT studies emphasize technical metrics such as power output enhancement, with limited attention given to the sustainability and environmental viability. This oversight restricts a comprehensive understanding of the ecological benefits and long-term potential of hybrid PV-TEG systems as sustainable energy technologies. Third, the limited consideration of diverse operational scenarios and the insufficient use of real-world data constrain the practical feasibility of current approaches. Real-life datasets are essential for connecting theoretical models with practical applications.

To fill these gaps, this study proposes an optimal energy harvesting strategy for hybrid PV-TEG systems under diverse operational scenarios with PSCs. Key contributions are concluded as follows.

1) A PV-TEG hybrid system is designed to enhance solar energy conversion, recycle waste heat, increase energy output density, and extend the operational lifespan of PV modules by integrating the strengths of PV and TEG components.

2) A chaotic RIME (c-RIME) optimizer is proposed for efficient power extraction from the PV-TEG hybrid system under challenging and complex environmental circumstances. This approach enhances overall MPPT performance, particularly in global convergence rate and accuracy.

3) Four case studies are conducted under varying

temperature and irradiance conditions for simulation tests. In addition, real atmospheric datasets measured in Hong Kong are utilized to verify the practical applicability of the proposed scheme, providing a thorough and realistic evaluation.

4) A more comprehensive evaluation framework is introduced to bridge gaps in previous studies, emphasizing both technical improvements and environmental considerations.

The remainder of this work is structured as follows. Section II covers the system modeling details, while Section III outlines the methodology design and implementation framework. Section IV analyzes case study results and Section V delivers a detailed techno-environmental evaluation. Finally, Section VI summarizes the contributions and highlights future research directions.

II. Mathematical Modelling

The hybrid PV-TEG system has been analyzed using various approaches, including thermodynamic evaluations. For instance, work in [9] investigates the theoretical modeling, reference [31] studies parallel PV-TEG setups with dual MPPT controllers to improve energy capture, and reference [32] reviews integration strategies through both experimental and numerical analyses to optimize system performance.

A. PV Modeling

A PV cell is modeled as an equivalent circuit comprising a photogenerated current source, parallel diodes, and resistances [33]. In practice, PV modules are arranged in arrays to meet specific power and voltage needs [34]. However, partial shading caused by weather conditions or physical obstructions reduces power output, triggers hotspot effects, and risks long-term damage. Shaded cells absorb excess energy, leading to efficiency loss and potential damage to the array.

To mitigate these challenges, bypass diodes are commonly deployed across PV strings, as demonstrated in Figs. 1(a) and (b). When reverse-biased, these diodes disconnect the shaded cells from the current path. However, this mechanism also introduces multi-peak features under PSCs, as shown in Figs. 1(c) and (d).

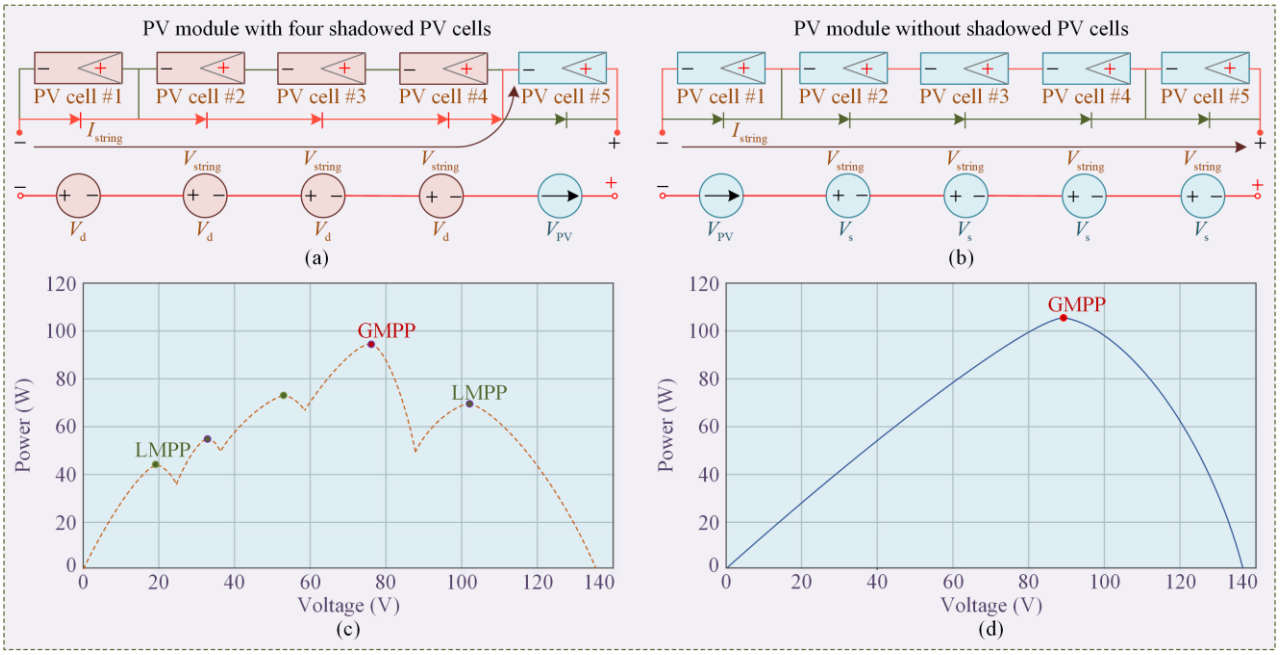

Fig. 1. Performance of PV modules under PSCs. (a) PV cells affected by shading. (b) PV cells operating without shading. (c) *P-V* characteristics under PSCs. (d) *P-V* characteristics under uniform illumination conditions.

The voltage of a shaded PV cell is restricted within certain predetermined boundaries, defined by [7]:

$$V_{\text{reverse}} = nV_{\text{oc}} + V_{\text{Bdiode}} \tag{1}$$

where V_{reverse} represents the reverse voltage across a partially shaded PV cell; V_{oc} signifies the open-circuit voltage; n means the PV cell number not covered by shading; and V_{Bdiode} represents the voltage drop across the diode.

At present, the most commonly used PV array topologies include series-parallel (SP) and total-cross-tied (TCT) configurations [35], [36]. The TCT topology is particularly recognized for its effectiveness in reducing power losses under PSCs, making it a widely studied and favored structure in PV power generation.

B. TEG Modeling

TEG modules, as shown in Fig. 2, produce electricity through thermoelectric units based on the Seebeck effect,

which is driven by the temperature gradient [37]. The open-circuit voltage is described by:

$$V_{oc} = \alpha \times \Delta T = \alpha (T_h - T_c) \tag{2}$$

where T_h and T_c represent the temperatures at the hot and cold ends, respectively; while α means the Seebeck coefficient.

It is worth noting that the Seebeck coefficient α used in (2) can be further expressed as a temperature-dependent function $\alpha(T_{av})$, as shown in (3). This formulation improves modeling accuracy by capturing the influence of the average temperature on thermoelectric conversion efficiency. Hence, the TEG characteristics can be presented more precisely by:

$$\alpha(T_{av}) = \alpha_0 + \alpha_1 \left(\frac{T_{av}}{T_0} \right) \tag{3}$$

where α_0 and α_1 represent two key components of α; T_{av} refers to the average temperature; and T_0 represents the reference temperature (usually 298.15 K).

Further, a typical TEG module's power output is expressed as [10]:

$$P_{TEG} = (\alpha \Delta T)^2 \times \frac{R_L}{(R_L + R_{TEG})^2} \tag{4}$$

where R_{TEG} refers to the internal resistance; and R_L indicates the load resistance.

In contrast to PV cells, TEG modules are typically configured in SP topology. This configuration facilitates efficient energy generation while enabling the optimization of power output [10]. The output current of the ith TEG module is calculated by:

$$I_i = \begin{cases} (V_{oci} - V_{Li}) \times \dfrac{I_{sci}}{V_{oci}} = I_{sci} - \dfrac{V_{Li}}{R_{TEGi}}, \\ \quad \text{if } 0 \leqslant V_{Li} \leqslant \dfrac{I_{sci}}{V_{oci}},\ i = 1,2,\cdots,N \\ 0, \text{otherwise} \end{cases} \tag{5}$$

where V_{oci}, V_{Li}, I_{sci}, and R_{TEGi} signify the open-circuit voltage, terminal voltage, short-circuit current, and internal resistance of the ith TEG module, respectively.

The power generated by a single TEG module i is calculated as:

$$P_{TEGi} = \begin{cases} V_{Li} I_i = I_{sci} V_{Li} - \dfrac{V_{Li}^2}{R_{TEGi}}, \\ \quad \text{if } 0 \leqslant V_{Li} \leqslant \dfrac{I_{sci}}{V_{oci}},\ i = 1,2,\cdots,N \\ 0, \text{otherwise} \end{cases} \tag{6}$$

The entire output power of a TEG array, obtained by summing the contributions of all individual modules, is given by:

$$P_{TEG\Sigma} = \sum_{i=1}^{N} P_{TEGi} \tag{7}$$

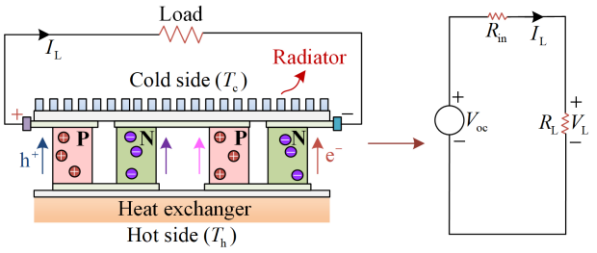

Fig. 2. Schematic of a typical TEG module.

C. PV-TEG System Modeling

The physical integration of PV and TEG modules allows direct thermal energy transfer between them, as illustrated in Fig. 3.

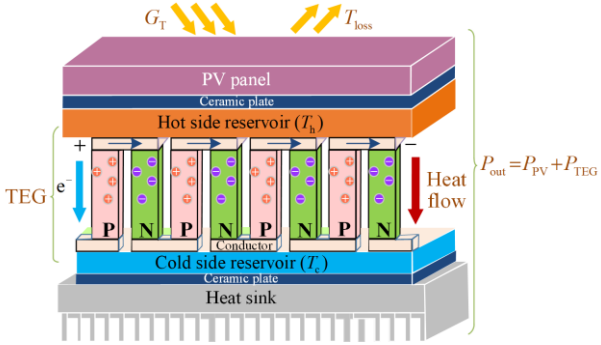

Fig. 3. Structural integration of a hybrid PV-TEG module.

In engineering applications, the SP connection is widely utilized but demonstrates certain limitations when applied to PV array layouts, particularly under PSCs. In contrast, TEG arrays employing the SP configuration remain adaptable and effective under NTD conditions. As a result, this study adopts TCT configurations for PV arrays and SP configurations for TEG arrays, as depicted in Fig. 4. In addition, the MPPT execution framework for the PV-TEG system is shown in Fig. 5.

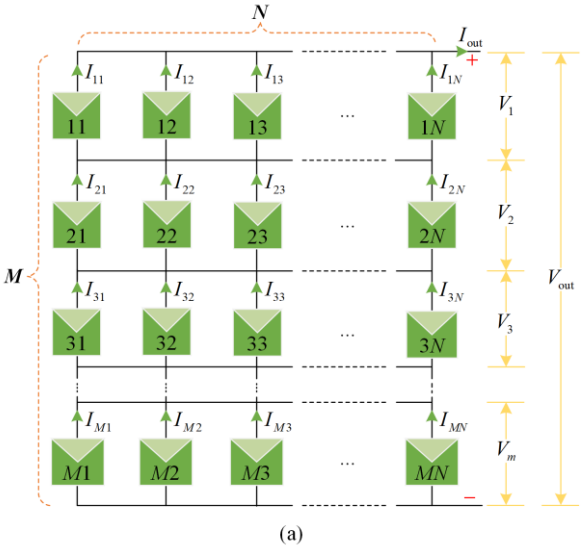

(a)

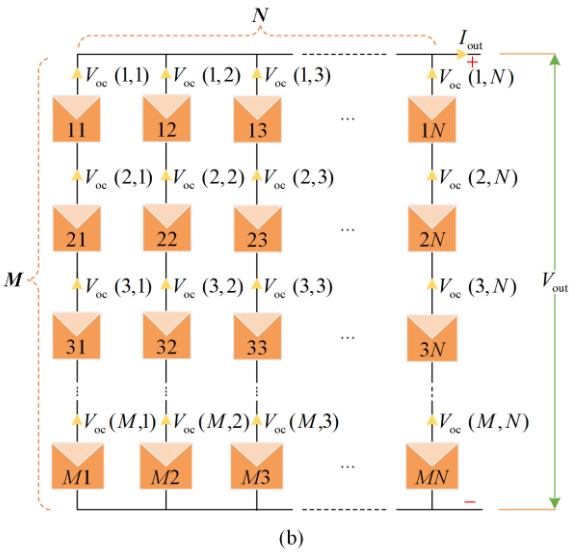

Fig. 4. Arrangement of PV and TEG arrays. (a) TCT configuration of a PV array with $M\times N$ modules. (b) SP configuration of a TEG array with $M\times N$ modules.

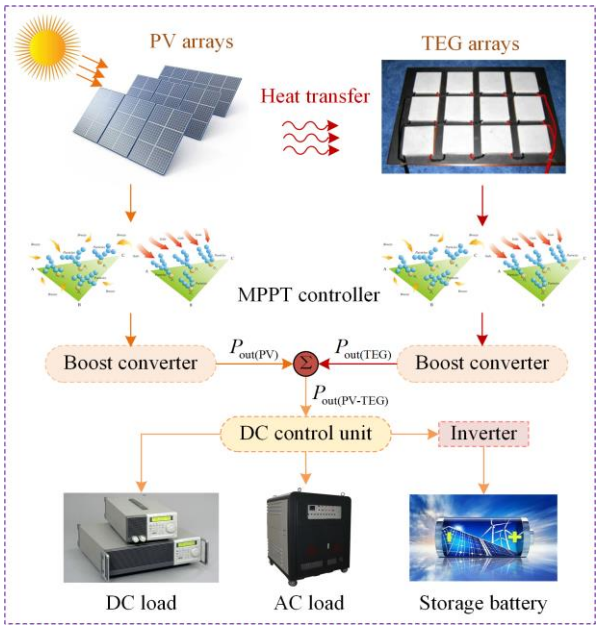

Fig. 5. MPPT structure for hybrid PV-TEG system.

In such a setup, waste heat from PV systems is effectively re-utilized by TEG modules. Meanwhile, TEG systems improve PV efficiency by offering a passive cooling mechanism, reducing the operating temperature of PV modules. This cooperative relationship, as detailed in [14], is described by a heat transfer equation that determines the hot-side temperature of the TEG module (T_{op}) using parameters such as ambient temperature (T_{am}), wind speed (W_s), and solar irradiance intensity (G_T), as follows [14]:

$$T_{op}=0.943T_{am}+0.028G_T-1.528W_s+4.3 \tag{8}$$

As depicted in Fig. 3, the TEG module's cold side temperature is equivalent to T_{am}. The total power output of this hybrid system is expressed by the sum of the output power of the PV subsystem (P_{PV}) and the TEG subsystem (P_{TEG}), as follows:

$$P_{PV\text{-}TEG}=P_{PV}+P_{TEG} \tag{9}$$

The overall efficiency of the PV-TEG hybrid system is given by [26]:

$$\eta_{PV\text{-}TEG}=\frac{P_{PV}+P_{TEG}}{G_T\times S_{PV}} \tag{10}$$

where S_{PV} means the area of PV board.

III. Methodology and MPPT Design

A. RIME Optimizer

The RIME optimizer is a nature-inspired optimization algorithm modeled after the process of rime ice formation. [38]. It replicates two distinct growth patterns: soft rime formation under gentle, variable winds, promoting broad exploration; and hard rime formation under strong, steady winds, enabling precise local exploitation. The corresponding searching behaviors of the soft and hard rimes are demonstrated in Figs. 6(a) and (b), respectively, where D_i $(i=1, 2, 3, 4)$ represents birth points of rime.

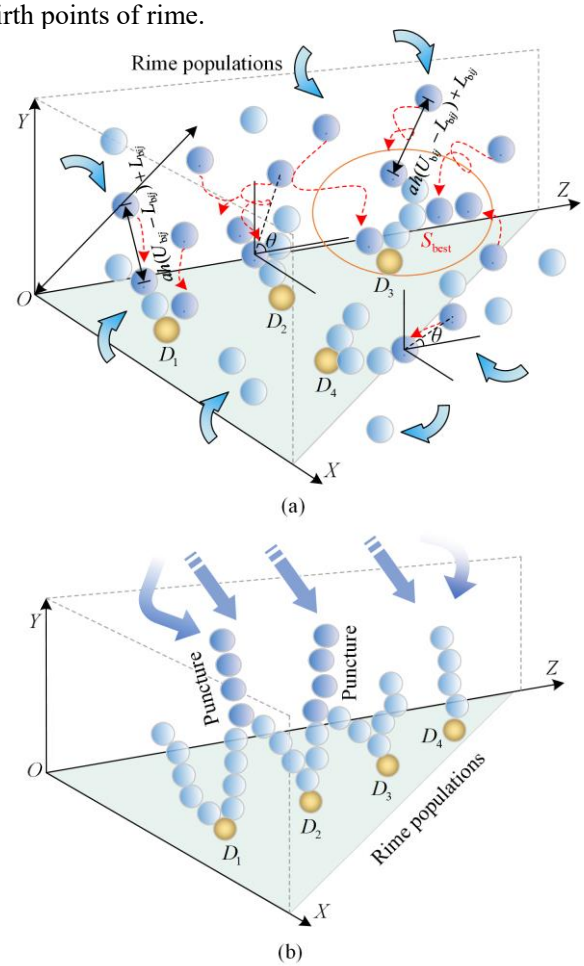

Fig. 6. Illustration of rime-based search mechanisms. (a) Soft rime. (b) Hard rime.

1) Rime Population Initialization

The initialization begins by forming the rime population $\boldsymbol{R}$, which consists of n individual rime agents, denoted as $\boldsymbol{A}_i$. Individual agent is then subdivided into d rime-particles, represented as x_{ij}. Mathematically, the rime population $\boldsymbol{R}$ and its agents are expressed as follows [38]:

$$\begin{cases} \boldsymbol{R} = \left[\boldsymbol{A}_1,\ \boldsymbol{A}_2,\ \cdots,\ \boldsymbol{A}_i\right]^{\mathrm{T}} \\ \boldsymbol{A}_i = \left[x_{i1},\ x_{i2},\ \cdots,\ x_{ij}\right] \end{cases} \tag{11}$$

$$\boldsymbol{R} = \begin{bmatrix} x_{11} & x_{12} & \cdots & x_{1j} \\ x_{21} & x_{22} & \cdots & x_{2j} \\ \vdots & \vdots & \vdots & \vdots \\ x_{i1} & x_{i2} & \cdots & x_{ij} \end{bmatrix} \tag{12}$$

2) Soft Rime Searching Strategy

Soft rime forms unpredictably under low wind speeds, facilitating wide search coverage. To model particle condensation and refine position updates, five distinct motion characteristics are considered, as illustrated in Fig. 6(a): 1) Particles wander randomly before condensation, influenced by environmental factors; 2) Particles condense when approaching existing agents, affecting their stability; 3) The adhesion distance varies among particles due to uneven condensation; 4) Particles beyond the effective radius do not condense; and 5) Agent growth increases with random condensation but eventually stabilizes due to environmental limits.

The updated particle position is determined as [38]:

$$\begin{aligned} R_{ij}^{\mathrm{new}} = R_{\mathrm{best},j} + r_1 \cos\theta \times \\ \beta(h \times (U_{\mathrm{b}ij} - L_{\mathrm{b}ij}) + L_{\mathrm{b}ij}),\ \ r_2 < E \end{aligned} \tag{13}$$

where R_{ij}^{new} indicates the updated position of particle j within agent i; $R_{\mathrm{best},j}$ represents the best position identified for particle j; the random factor r_1, ranging from −1 to 1, along with $\cos\theta$, governs the movement direction and evolves over iterations in (14); the environmental factor β varies with the iteration count to simulate external conditions and guarantee algorithmic convergence, as detailed in (15); $U_{\mathrm{b}ij}$ and $L_{\mathrm{b}ij}$ denote the upper and lower bounds of the escape space for particle j within agent i, respectively; r_2 is a random number based on the adhesion coefficient threshold E, which influences the likelihood of agent condensation and grows progressively with each iteration; and the adhesion degree h is a randomly generated value ranging between 0 and 1.

$$\theta = \pi \times \frac{t}{10T} \tag{14}$$

$$\beta = 1 - \frac{wt}{T} \Big/ w \tag{15}$$

$$E = \sqrt{(t/T)} \tag{16}$$

where t and T are current and maximum iterations, respectively; while w denotes a predefined constant set to 5, used to control the step function segmentation.

3) Hard Rime Puncture Mechanism

Hard rime develops under strong wind conditions, promoting precise local exploitation. This mechanism exchanges particles across agents to refine solutions and prevent entrapment in local optima. The process is depicted in Fig. 6(b), and the particle exchange is governed by [38]:

$$R_{ij}^{\mathrm{new}} = R_{\mathrm{best},j},\ \ r_3 < F^{\mathrm{normr}}(S_i) \tag{17}$$

where F^{normr} represents the normalized fitness score of the current agent; while r_3 means a random number within (−1, 1); and S_i represents the ith rime agent.

4) Positive Greedy Selection Mechanism

This mechanism evaluates agents by comparing fitness values before and after updates, retaining those with superior quality. It dynamically adjusts agent positions, guiding the population toward optimal solutions and enhancing global search efficiency. The overall execution framework of the RIME optimizer is summarized in Table I.

TABLE I
PSEUDO-CODE OF RIME OPTIMIZER

```
Initialize the rime population R
Identify the current best agent and compute its fitness value
While t ⩽ T
Compute the adherence coefficient E using Eq. (16)
  If r2 < E
  Update rime positions using the soft-rime strategy based on Eq. (13)
  End If
  If r3 > Normalize fitness of Si
  Apply the hard-rime strategy using Eq. (17)
  End If
If F(Ri^new) < F(Ri)
Solution comparison and update via positive greedy selection
  End If
  t = t + 1
End while
```

B. Chaotic RIME Optimizer

Population initialization is a critical factor influencing the efficiency of meta-heuristic algorithms. In the absence of prior information, RIME commonly employs random initialization, which may lead to uneven population distribution, limited diversity, and slower convergence. Chaos mapping [39], known for its randomness and sensitivity, enhances solution diversity and helps avoid local optima. Among various chaotic maps, Logistic, Tent, and Circle mappings are widely utilized in algorithm design. Circle mapping stands out for its stability and broad distribution of chaotic values. However, its tendency to concentrate values between 0.2 and 0.6 limits its uniformity. To address this issue, an enhanced Circle mapping has been developed for a

more even distribution. The original Circle chaos mapping is expressed as [40]:

$$x_{n+1} = \mathrm{mod}\left(x_n + 0.2 - \frac{0.5}{2\pi}\sin(2\pi x_n), 1 \right) \quad (18)$$

where mod(·) represents the modulo operation, which keeps the output within the range [0,1) to ensure normalized chaotic sequences; and n denotes the dimensionality of the solution.

The improvement can be formulated as:

$$x_{n+1} = \mathrm{mod}\left(3.85x_n + 0.4 - \frac{0.7}{3.85\pi}\sin(3.85\pi x_n), 1 \right) \quad (19)$$

Figure 7 visualizes the two-dimensional distribution of the initialized population under Logistic, Tent, and the improved Circle mapping, respectively. Each point represents an individual, with its x and y coordinates denoting normalized values along two dimensions of the search space.

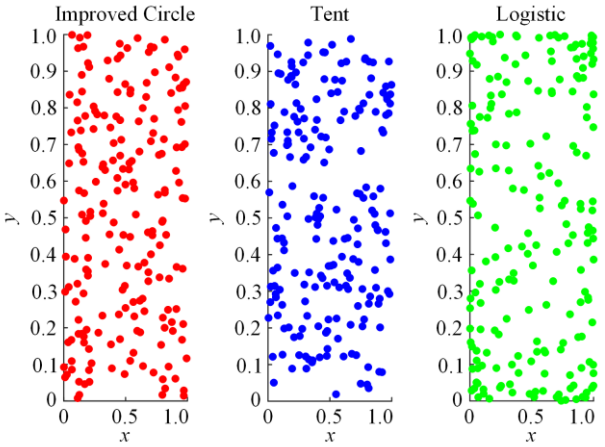

Fig. 7. Comparison of population initialization distributions using three different chaos mapping techniques.

Logistic mapping exhibits a relatively uniform probability distribution in the central range but shows higher probabilities at the extremes, which limits its effectiveness in locating global optima. Tent mapping demonstrates good ergodicity, yet suffers from short cycles and unstable periodic points, compromising its overall stability. In contrast, the improved Circle mapping achieves a more uniform and stable distribution, making it an optimal choice for initializing the RIME population. Therefore, this study adopts the improved Circle mapping for RIME population initialization to enhance distribution quality and strengthen global search capabilities.

C. MPPT Design for PV-TEG System

1) Objective Function Design

The voltage outputs of PV and TEG systems act as optimization variables. The fitness functions are defined as:

$$\begin{aligned} &\min f(V_{\mathrm{PV}}) = -P_{\mathrm{out}}(V_{\mathrm{PV}}) = -V_{\mathrm{PV}} I_{\mathrm{PV}}(V_{\mathrm{PV}}), \\ &\text{s.t.} \quad V_{\mathrm{PV}}^{\min} \leqslant V_{\mathrm{PV}} \leqslant V_{\mathrm{PV}}^{\max} \end{aligned} \quad (20)$$

where $P_{\mathrm{out}}(V_{\mathrm{PV}})$ denotes the PV system's power; while $V_{\mathrm{PV}}^{\min}$ and $V_{\mathrm{PV}}^{\max}$ represent its operational voltage limits.

Similarly, for TEG systems, there are:

$$\begin{aligned} &\min f(V_{\mathrm{TEG}}) = -P_{\mathrm{out}}(V_{\mathrm{TEG}}) = -V_{\mathrm{TEG}} I_{\mathrm{TEG}}(V_{\mathrm{TEG}}), \\ &\text{s.t.} \quad V_{\mathrm{TEG}}^{\min} \leqslant V_{\mathrm{TEG}} \leqslant V_{\mathrm{TEG}}^{\max} \end{aligned} \quad (21)$$

where $P_{\mathrm{out}}(V_{\mathrm{TEG}})$ represents the TEG system's power; while $V_{\mathrm{TEG}}^{\min}$ and $V_{\mathrm{TEG}}^{\max}$ set its operational voltage range.

2) Boost Converter Model

MPPT technique adjusts the boost converter's duty cycle (D_c) to optimize power output [41]. Figure 8 illustrates the integration of the c-RIME-based MPPT scheme with a boost converter, where $V_{\text{PV-TEG}}$ represents the system's output voltage; while V_{out} is the improved voltage via the boost circuit; parameter f indicates the switching frequency; the standard and maximum currents flowing through the inductor L are denoted as I_{L} and $I_{\mathrm{L\,max}}$, respectively.

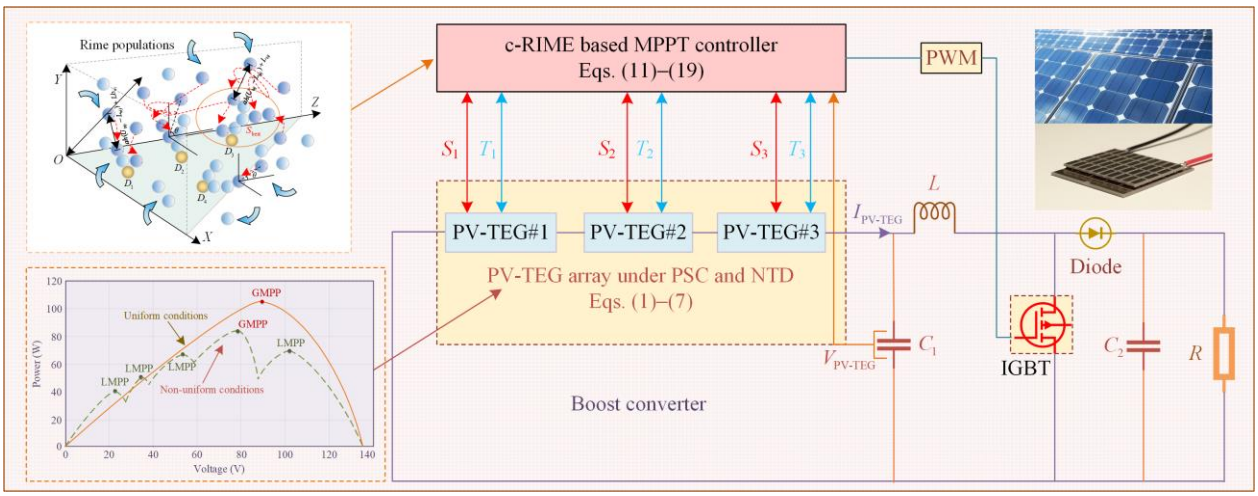

Fig. 8. MPPT strategy based on c-RIME for PV-TEG system under PSCs.

Specifically, V_{out}, L, and the filter capacitance C_1, are calculated as:

$$V_{out} = \frac{V_{PV\text{-}TEG}}{1 - D_c} \tag{22}$$

$$L = \frac{V_{out}}{4 I_{Lmax} \times f} \tag{23}$$

$$C_1 = L \times \frac{(I_L + I_{Lmax}/2)^2 - (I_L - I_{Lmax}/2)^2}{(V_{in} + 0.005V_{in})^2 - (V_{in} - 0.005V_{in})^2} \tag{24}$$

where V_{in} is the input voltage of the boost converter. Key parameters for the PV and TEG systems are detailed in Table II.

TABLE II
CRITICAL PARAMETERS OF BOOST CIRCUITS

Parameter	PV system	TEG system
Capacitor (μF)	$C_1 = C_2 = 1$	$C_1 = 66, C_2 = 200$
Inductor L (mH)	500	250
Resistive load R (Ω)	200	10
Switching frequency (kHz)	100	$f_s = 20$

MPPT efficiency is calculated using:

$$\eta_{MPPT} = \frac{P_{PV\text{-}TEG}(t)}{P_{max}(t)} \times 100\% \tag{25}$$

where $P_{PV\text{-}TEG}(t)$ and $P_{max}(t)$ denote the real power and the maximum power of the hybrid system at time t, respectively.

3) MPPT Execution Framework

Building on the previous discussion, Fig. 9 illustrates the implementation steps for the designed MPPT strategy, aiming to optimize power output while minimizing the adverse effects of PSCs.

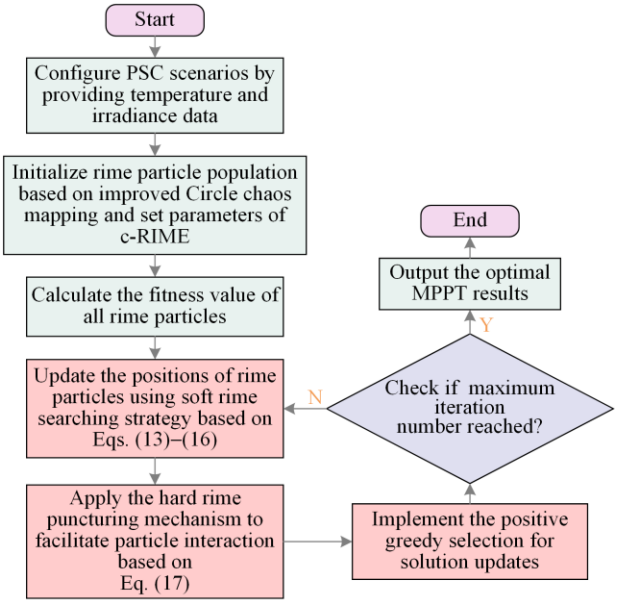

Fig. 9. MPPT execution structure using c-RIME under PSCs.

IV. CASE STUDIES

This section evaluates the proposed c-RIME-based power extraction strategy across different operating scenarios, including startup test, stepwise solar irradiation variations, stochastic fluctuations, and real-world scenarios using atmospheric data from Hong Kong. Extreme conditions are simulated by applying partial shading factors of 1, 0.6, and 0.3 across three PV-TEG modules, validating the algorithm's global optimization capabilities, particularly under randomized and real-world operating dynamics. All simulations are carried out utilizing the Matlab/Simulink 2022a platform on a high-performance personal computer, equipped with an Intel Core 3.0 GHz TMi9 CPU with 128 GB RAM.

For comparison, the proposed method is benchmarked against P&O and eight other well-established algorithms, including reptile search algorithm (RSA) [42], multi-verse optimization (MVO) [43], moth-flame optimization (MFO) [44], sine cosine algorithm (SCA) [45], and three algorithms from previous studies on this research topic, i.e., AOA [28], AOS [29], and SSA [30]. To ensure fair comparison, the population size (N_p) is uniformly set to 10, and the maximum iteration count (k_{max}) is fixed at 5. For P&O, the step size is configured as 10^{-7}. Table III provides the key system parameters.

TABLE III
KEY PARAMETERS OF PV-TEG HYBRID SYSTEM

	Parameter	Setting
PV module	Type	User-defined
	Typical peak power (W)	213.15
	MPP voltage (V)	29.00
	MPP current (A)	7.35
	Short-circuit current I_{sc} (A)	7.84
	Open-circuit voltage V_{oc} (V)	36.30
	Temperature coefficient of $I_{sc}(k_1)$ (mA/°C)	3
TEG module	Type	TGM199-1.4-2.0
	Parameter measurement conditions T_c and T_h (°C)	30 and 200
	Component dimensions (mm×mm×mm)	40×40×4.4
	Typical peak power (W)	7.3
	I_{sc} (A)	2.65
	V_{oc} (V)	11
	Number of thermoelectric units	200

A. Startup Test

This test replicates real-world shading effects caused by objects or clouds, resulting in uneven irradiance across PV modules. It evaluates the responsiveness and stability of the MPPT scheme in tracking and maintaining GMPP under PSCs. To simulate these effects, solar irradiances for three PV arrays are assigned as 800 W/m², 600 W/m², and 700 W/m², respectively, with the ambient

temperature held at 25°C. The hot side temperatures of the TEG modules are computed using (8).

Figure 10 compares the performance of nine MPPT algorithms, showing that c-RIME achieves faster and more stable convergence to GMPP and yields higher energy output than other methods. Figure 10(b) highlights its superior responsiveness in maximizing energy harvesting, while Fig. 10(a) confirms its consistent and stable power convergence, which is critical for ensuring system reliability under dynamically changing environmental conditions.

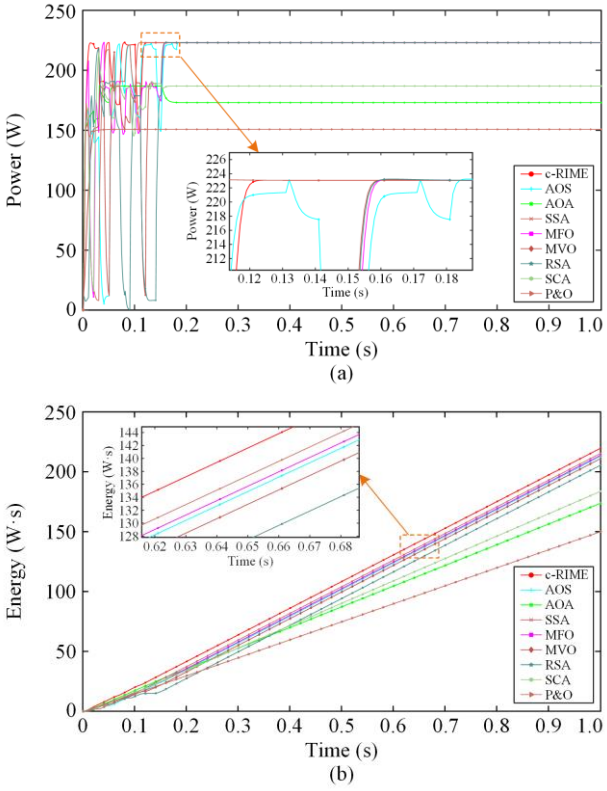

Fig. 10. Performance comparison of nine MPPT methods during startup. (a) Generated power. (b) Accumulated energy.

B. Stepwise Variations in Solar Irradiation

This test evaluates the impact of rapid cloud movement on the energy output of hybrid PV-TEG modules. Ambient temperature is set at 25°C with wind speed W_s fixed at 1.5 m/s. Solar irradiation changes stepwise across PV panels (as shown in Fig. 11), adjusting TEG hot side temperatures via (8).

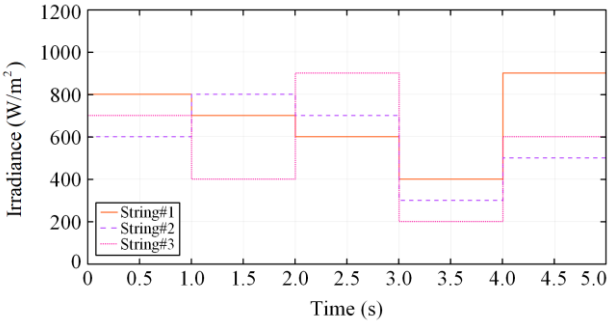

Fig. 11. Solar irradiation variations in steps under PSCs.

Figure 12(a) shows that c-RIME maintains higher and more stable power output compared to benchmark methods, with strong adaptability to sudden changes in irradiance. As illustrated in Fig. 12(b), c-RIME consistently maximizes energy output throughout the test period. Notably, between 1.95 s and 2.25 s, c-RIME exhibits a significant advantage in energy accumulation, proving its effectiveness during transient weather conditions. These results confirm c-RIME's superior adaptability and dynamic optimization capability under step-changing changes.

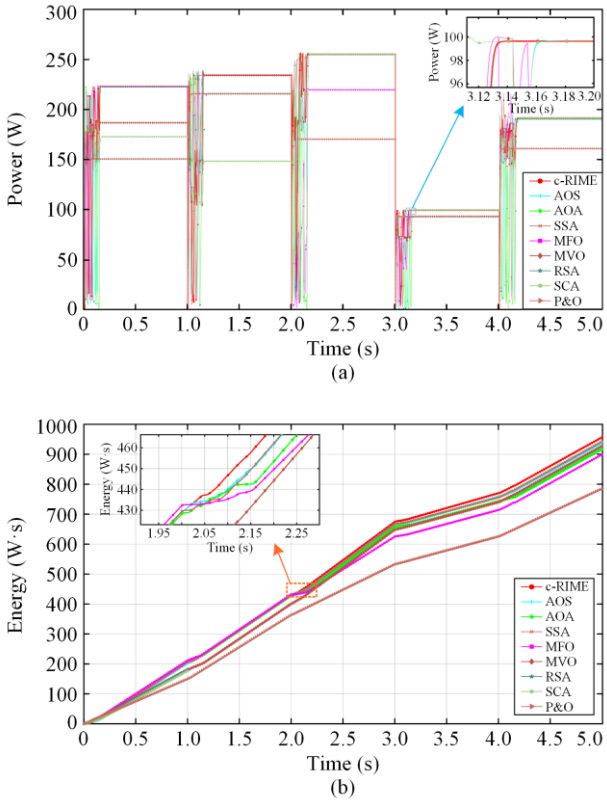

Fig. 12. Performance comparison of nine MPPT methods during stepwise variations. (a) Generated power. (b) Accumulated Energy.

C. Stochastic Change in Solar Irradiation

This test mimics summer conditions with fluctuating solar irradiance over a 12-hour cycle, as illustrated in Fig. 13. The hot side of the TEG modules experiences both steady and randomly varying thermal profiles, while wind speed (W_s) varies from 1 m/s to 10 m/s, reflecting real environmental dynamics. The simulation aims to evaluate MPPT algorithms on responsiveness, adaptability, and efficiency under unpredictable conditions.

Figure 14(a) shows that c-RIME consistently achieves higher power outputs, especially during peak irradiance (13:00–15:00), highlighting its superior solar

energy conversion efficiency. Figure 14(b) confirms c-RIME's superiority in energy accumulation, surpassing other algorithms throughout the day. Notably, during the midday (10:00–11:00), c-RIME remains stable and efficient despite rapid environmental changes, validating its robustness and reliability in handling stochastic conditions.

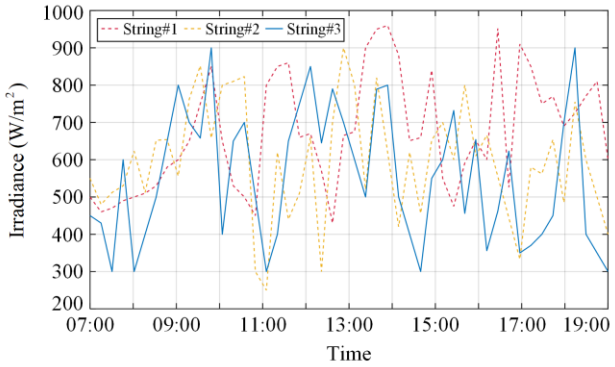

Fig. 13. Stochastic irradiation changes.

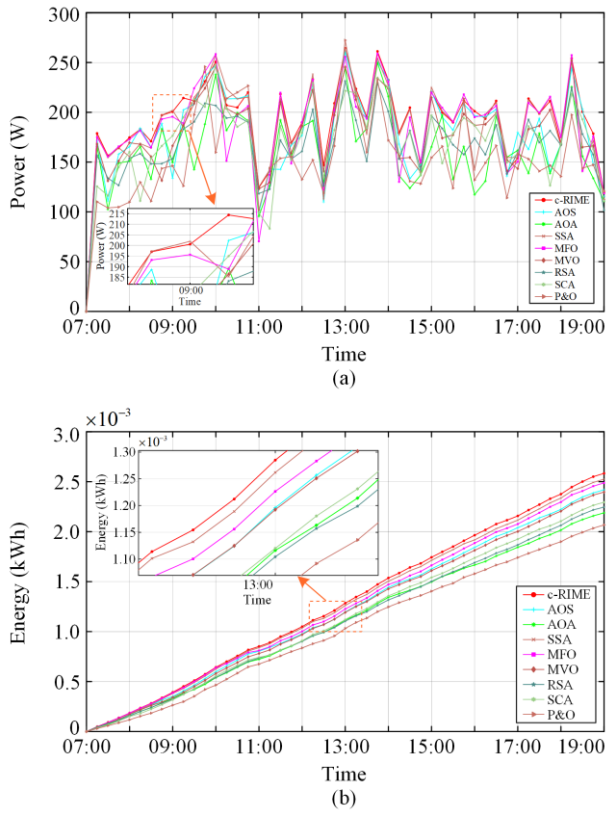

Fig. 14. Performance comparison of nine MPPT methods during stochastic change. (a) Generated power. (b) Accumulated energy.

D. Field-measured Temperature and Solar Irradiation Data in Hong Kong

To further assess real-world applicability, this study evaluates MPPT algorithm performance based on solar irradiance and temperature data recorded in 2022 over four representative days in Hong Kong, sampled at ten-minute intervals. Unlike controlled simulations, real-world datasets introduce natural variability and complexity, offering a robust test for algorithm adaptability. Situated at 22.3°N, 114.2°E, Hong Kong's subtropical climate features hot, humid summers (26–33 °C) and mild, dry winters (10–20 °C), making it ideal for assessing performance across diverse conditions. To replicate PSCs, the irradiance levels of three PV panels are set to 100%, 60%, and 30% of the recorded values, reflecting gradual, long-term changes. Wind speed (W_s) ranges from 1 m/s to 10 m/s. Figure 15(a) illustrates irradiance data from four seasonal days in Hong Kong, while Fig. 15(b) shows relevant ambient temperature changes. Figures 16 and 17 compare power and energy outputs obtained by various MPPT methods. As seen, under all testing days, c-RIME always outperforms other algorithms, proving its adaptability, efficiency, and reliability under fluctuating solar irradiance and temperature.

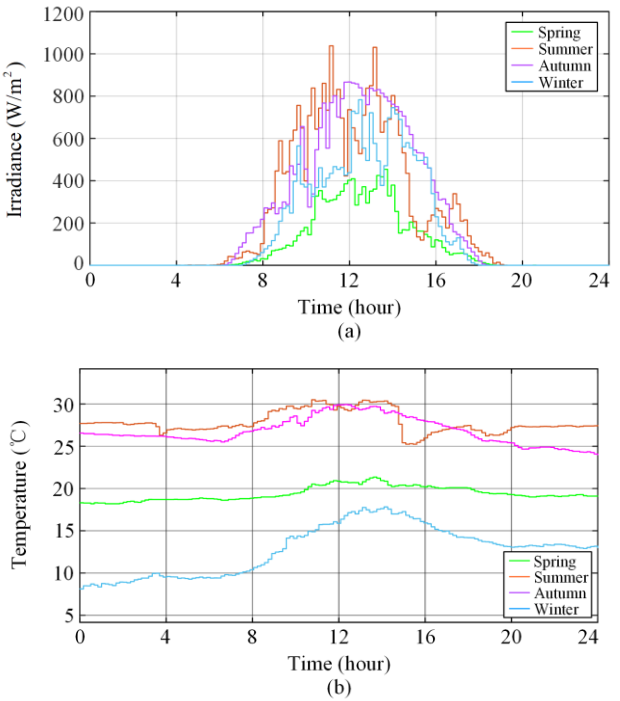

Fig. 15. Variations in temperature and solar irradiation over four representative days in Hong Kong. (a) Solar irradiation levels. (b) Temperature trends.

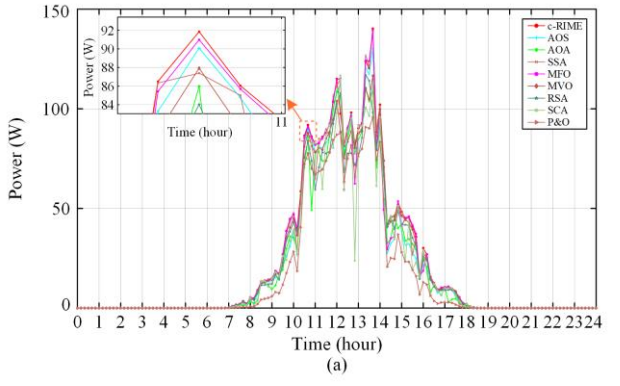

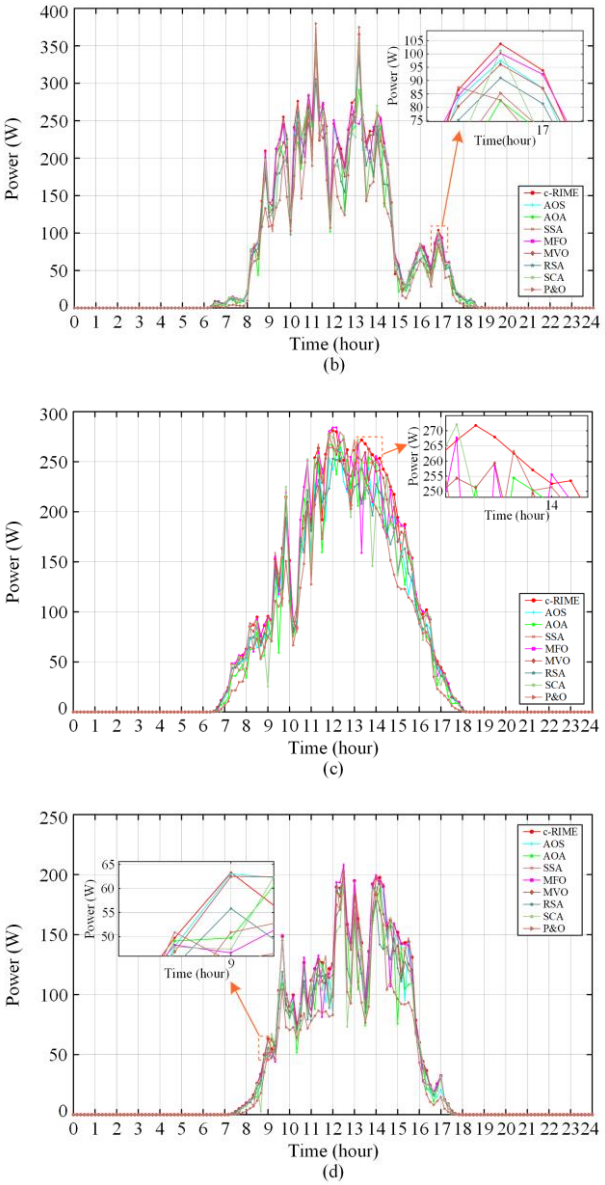

Fig. 16. Power generation across four representative days in Hong Kong. (a) Spring. (b) Summer. (c) Autumn. (d) Winter.

In spring, when weather conditions are mild and variable, c-RIME delivers higher power output than other methods, highlighting its superior adaptability. In summer, characterized by high solar irradiance, all methods achieve increased power, but c-RIME stands out with the highest output. The seasonal energy output comparisons in Fig. 17 further validate that c-RIME consistently maximizes energy harvesting across all scenarios, emphasizing its optimization effectiveness and generalizability under a wide range of environmental conditions.

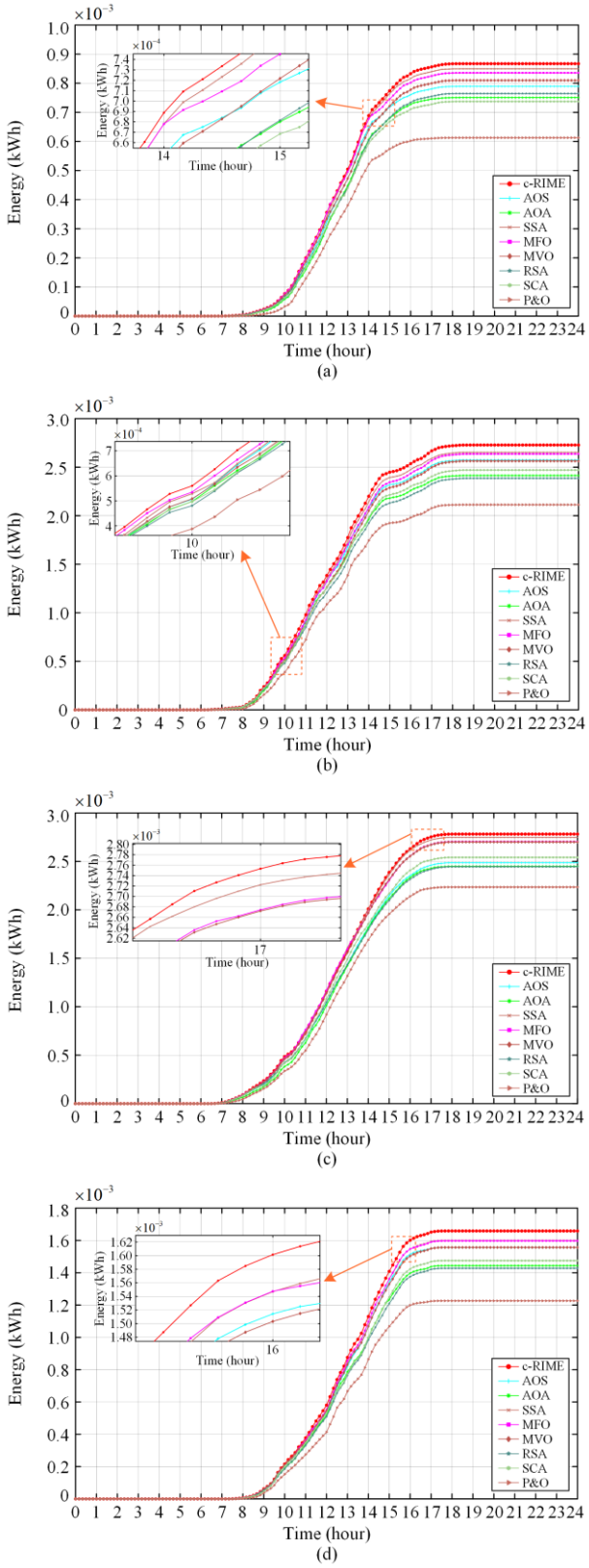

Fig. 17. Energy output recorded on four representative days in Hong Kong. (a) Spring. (b) Summer. (c) Autumn. (d) Winter.

E. Robustness Evaluation Under Environmental Uncertainty

To further evaluate the robustness and generalizability of the proposed algorithm under diverse operating scenarios, a series of uncertainty tests is conducted by introducing controlled variations in temperature and solar irradiance. To assess the impact of changing environmental conditions on the MPPT performance of different algorithms, three evaluation metrics are adopted: average power output $P_{\text{out}}^{\text{avg}}$, maximum variability $\Delta v^{\max}$, and average variability Δv^{avg}.

1) Temperature Variation Test

To isolate the impact of temperature, the baseline solar irradiance is fixed at 600 W/m², while the ambient temperature is varied from 0 ℃ to 40 ℃ in increments of 5 ℃. As shown in Fig. 18(a), the average power output of all algorithms generally decreases as temperature increases, though the rate and stability of this decline vary significantly. Among them, P&O, as a traditional deterministic method, exhibits the most pronounced drop, whose output falls from 68.89 W to 41.49 W, indicating its severe vulnerability to temperature-induced perturbations. This stems from its fixed-step search strategy, which lacks adaptability to dynamic PV-TEG characteristics under varying thermal conditions. Other meta-heuristic algorithms, such as MVO and RSA, also experience notable decreases. For instance, RSA declines from 74.17 W to 63.55 W, marking a 14.32% reduction. In contrast, the proposed c-RIME algorithm maintains a stable and high-power output throughout the variations, with its output decreasing only modestly from 75.55 W to 73.48 W (a reduction of 2.74%). This resilience is attributed to its dual-phase rime-inspired search mechanism and chaotic initialization, which enhance its ability to resist thermal-induced local optima and maintain better global search behavior.

Figure 18(b) presents the maximum variability in output power under different temperature levels. It can be seen that the proposed c-RIME demonstrates well-controlled behavior. In particular, after the temperature intensity ratio surpasses 50%, its variability gradually levels off and remains at a low level across the high-temperature range. This trend indicates strong convergence stability, and resistance to external disturbance. It is also noteworthy that P&O maintains an almost flat variability curve, with both maximum and average variability values approaching zero throughout the entire test. This reflects a lack of dynamic response capability, as it is prone to quickly settle near the initial LMPP and fails to track changes. This results in consistently low power output and negligible fluctuation, not due to robustness, but rather to stagnation.

The trend of average variability is shown in Fig. 18(c), where AOA shows relatively lower and more stable average variability values, particularly in the mid-temperature. However, it is important to note that AOA's average power output is significantly lower than that of c-RIME across nearly all temperature levels, reflecting weaker tracking performance overall. In contrast, c-RIME achieves a comparably low level of average variability with small fluctuations, while also maintaining higher power output across all temperatures. Overall, c-RIME can achieve a well-balanced performance.

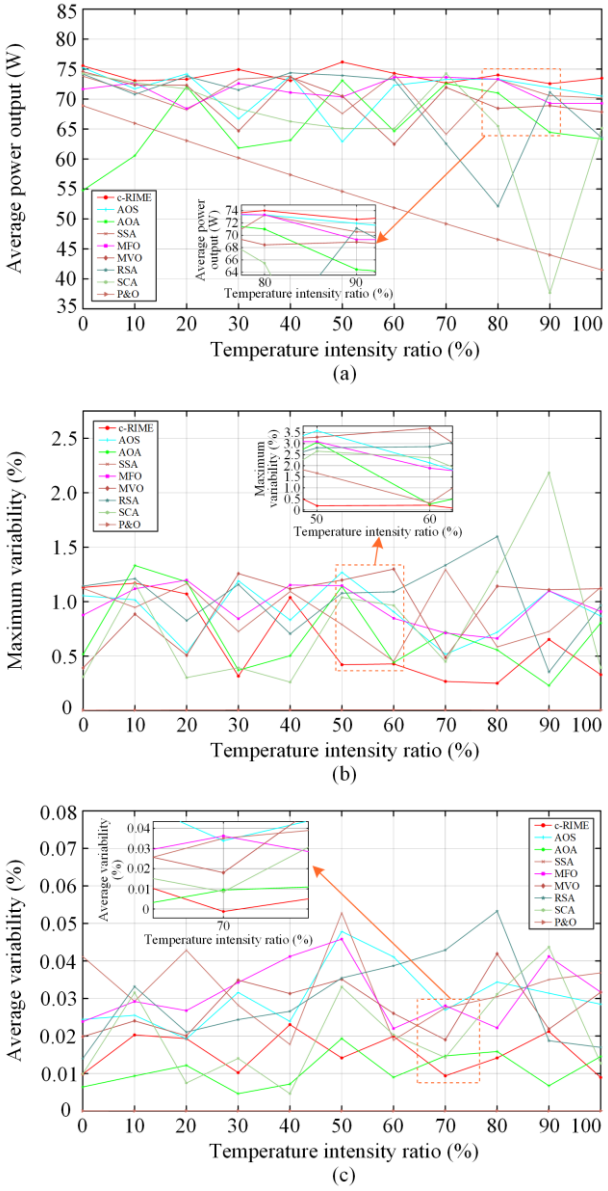

Fig. 18. Performance comparison under temperature variation. (a) Average power output. (b) Maximum variability. (c) Average variability.

2) Irradiance Variation Test

To assess the adaptability of different algorithms under changing solar irradiance conditions, this test varies the irradiance intensity ratio from 0–1000 W/m^2 in 5% increments, while maintaining a constant ambient temperature of 25 ℃.

Figure 19(a) shows that all algorithms follow a monotonic increase in average power output as irradiance rises, which is consistent with the expected correlation between solar input and energy harvesting potential. Across the entire irradiance range, c-RIME consistently maintains high output levels and emerges as the clear leader when the irradiance intensity ratio exceeds 80%. This confirms c-RIME's superior capability in GMPP tracking, especially under full sunlight conditions, where search precision and convergence reliability are critical. It is also noteworthy that SCA demonstrates a clear drop in output around the 70% irradiance point, indicating a possible convergence failure or misjudgment of the optimal point. Figures 19(b) and (c) show the maximum and average variability of power output under different irradiance levels.

Most meta-heuristic methods, including AOA, RSA, SCA, and AOS, present moderate to high variability, particularly in the low-irradiance stage (5%–30%), where limited energy input and weaker MPP signals challenge search efficiency. For instance, the average variability of RSA increases sharply by 95.02% from 0 to 10% irradiance. P&O appears to have very low variability in both maximum and average terms, largely due to their tendency to fall into local optima early. In contrast, c-RIME maintains both low magnitude and smooth trends in variability across most of the irradiance spectrum. Although c-RIME experiences a brief increase in maximum variability during the mid-range irradiance interval (50%–60%), its values remain relatively low compared to those of other algorithms across the full irradiance range. Regarding average variability, c-RIME exhibits a more stable trend as irradiance increases, and maintains consistently low values without any abrupt fluctuations.

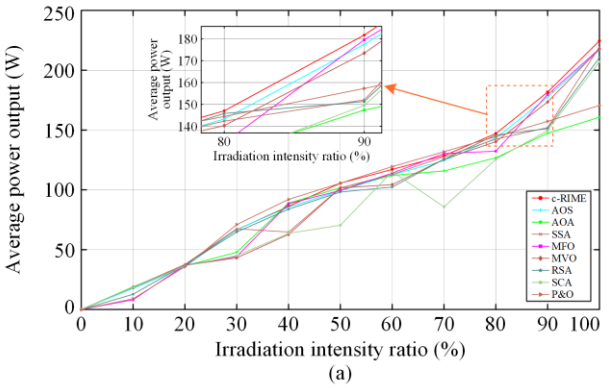

(a)

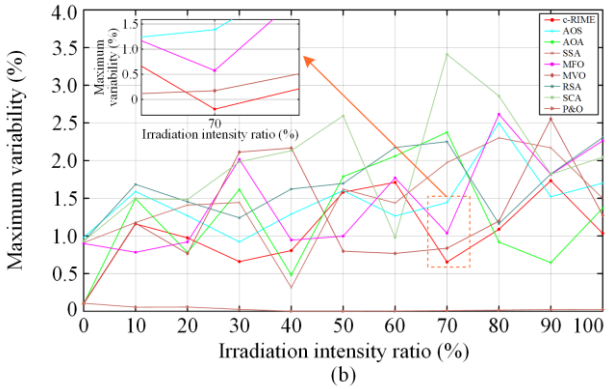

(b)

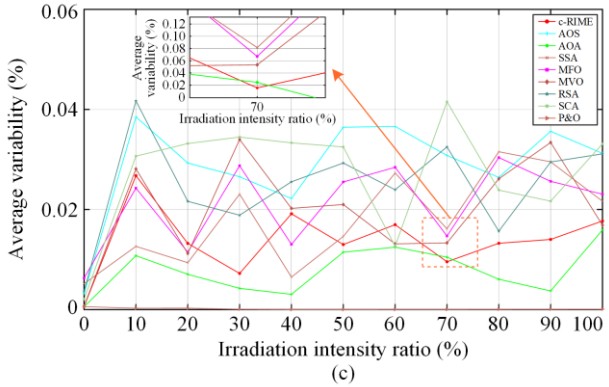

(c)

Fig. 19. Performance comparison under irradiance variation. (a) Average power output. (b) Maximum variability. (c) Average variability.

V. Techno-Environmental Assessment

This section assesses the energy performance of the PV-TEG system after MPPT and evaluates its environmental benefits through carbon emission analysis.

A. Technical Assessment

The technical analysis focuses on energy output as the key indicator of MPPT performance across various conditions. Furthermore, system stability is evaluated using two metrics: the maximum and average power fluctuations, defined as:

$$\Delta v^{\max} = \max_{t=2,3,\cdots,T} \frac{\left|P_{\text{out}}(t) - P_{\text{out}}(t-1)\right|}{P_{\text{out}}^{\text{avg}}} \tag{26}$$

$$\Delta v^{\text{avg}} = \frac{1}{T-1}\sum_{t=2}^{T} \frac{\left|P_{\text{out}}(t) - P_{\text{out}}(t-1)\right|}{P_{\text{out}}^{\text{avg}}} \tag{27}$$

where T is the total operation time; t is the current time step; $P_{\text{out}}(t)$ and $P_{\text{out}}(t-1)$ denote the PV-TEG system power output at the current and preceding time steps, respectively; and $P_{\text{out}}^{\text{avg}}$ is the average power output of the PV-TEG system.

A summary of energy outputs and fluctuation metrics for eight MPPT methods is provided in Table IV. The P&O method is excluded from the fluctuation analysis due to its tendency to converge prematurely, resulting in

misleadingly low fluctuations. This exclusion is supported by data from Figs. 10, 12, 14, 16, and 17, which consistently show that P&O delivers the lowest energy outputs among the tested methods.

TABLE IV
STATISTICAL RESULTS OF VARIOUS METHODS UNDER FOUR CASE STUDIES

Testing scenarios		Indicators	SCA	RSA	MVO	MFO	SSA	AOA	AOS	c-RIME
Start-up test		Energy (W·s)	183.74	205.54	211.03	213.82	215.44	173.47	212.99	219.72
		Δv^{max} (%)	30.0100	34.6369	35.1643	21.1106	32.3056	39.4998	26.7512	12.9878
		Δv^{avg} (%)	0.2310	0.4550	0.4580	0.3053	0.1757	0.2004	0.3527	0.1513
Stepwise variations in solar irradiation		Energy (W·s)	830.83	906.44	928.42	900.4781	943.98	918.03	939.64	957.72
		Δv^{max} (%)	34.6273	34.4243	23.4959	26.7158	26.3940	33.0741	28.9016	20.2471
		Δv^{avg} (%)	0.5496	0.5682	0.3419	0.4774	0.4927	0.7601	0.5893	0.3203
Stochastic change in solar irradiation		Energy (kWh)	2.2945×10^{-3}	2.2459×10^{-3}	2.3969×10^{-3}	2.4881×10^{-3}	2.5257×10^{-3}	2.1886×10^{-3}	2.4194×10^{-3}	2.5834×10^{-3}
		Δv^{max} (%)	35.5567	37.4670	30.1188	26.8605	24.9954	31.0313	29.6441	22.5967
		Δv^{avg} (%)	1.4053	1.4129	0.9026	0.4280	0.3557	0.3973	0.6630	0.3383
Field measured temperature and solar irradiation data in Hong Kong	Spring	Energy (kWh)	0.7373×10^{-3}	0.7646×10^{-3}	0.8099×10^{-3}	0.8357×10^{-3}	0.8476×10^{-3}	0.7506×10^{-3}	0.7891×10^{-3}	0.8672×10^{-3}
		Δv^{max} (%)	7.9207	6.2128	6.9227	10.9795	8.3556	5.3814	11.5727	9.7217
		Δv^{avg} (%)	0.0480	0.0776	0.0431	0.0548	0.0397	0.0214	0.0735	0.0382
	Summer	Energy (kWh)	2.4708×10^{-3}	2.3860×10^{-3}	2.5637×10^{-3}	2.6361×10^{-3}	2.6537×10^{-3}	2.4150×10^{-3}	2.5750×10^{-3}	2.7287×10^{-3}
		Δv^{max} (%)	7.1022	4.9077	5.5565	6.8977	6.5836	4.8425	9.5050	9.2736
		Δv^{avg} (%)	0.0459	0.0699	0.0324	0.0354	0.0421	0.0285	0.0618	0.0485
	Autumn	Energy (kWh)	2.5415×10^{-3}	2.4456×10^{-3}	2.7005×10^{-3}	2.7045×10^{-3}	2.7481×10^{-3}	2.4499×10^{-3}	2.4869×10^{-3}	2.7826×10^{-3}
		Δv^{max} (%)	9.7391	6.7597	7.4047	9.1448	9.0798	5.8054	6.9300	8.9688
		Δv^{avg} (%)	0.0571	0.0917	0.0492	0.0435	0.0404	0.0440	0.0888	0.0397
	Winter	Energy (kWh)	1.4748×10^{-3}	1.4279×10^{-3}	1.5568×10^{-3}	1.5977×10^{-3}	1.6011×10^{-3}	1.4441×10^{-3}	1.5569×10^{-3}	1.6586×10^{-3}
		Δv^{max} (%)	10.5568	7.3548	8.1969	11.3000	8.1821	6.8893	13.5449	9.1496
		Δv^{avg} (%)	0.0628	0.0949	0.0524	0.0499	0.0397	0.0369	0.0872	0.0340

For reference, P&O achieves energy outputs of 149.99 W·s and 786.09 W·s in the startup test and stepwise variation scenarios, respectively. Under stochastic changes and seasonal conditions (spring, summer, autumn, and winter), its energy outputs are recorded as 2.0679×10^{-3} kWh, 0.6128×10^{-3} kWh, 2.1135×10^{-3} kWh, 2.2351×10^{-3} kWh, and 1.2263×10^{-3} kWh, respectively. The specific results are tabulated in Table IV. It can be observed that c-RIME consistently delivers the highest energy output across all scenarios, highlighting its superior capability for optimizing energy conversion. For instance, during the startup test, c-RIME achieves 146.49%, 119.58%, 106.90%, 104.12%, 102.76%, 101.99%, 126.67%, and 103.16% of the energy output compared to P&O, SCA, RSA, MVO, MFO, SSA, AOA, and AOS, respectively. Similarly, during winter conditions, c-RIME reaches 135.25%, 112.46%, 116.16%, 106.54%, 103.81%, 103.59%, 114.85%, and 106.53% of the output obtained by these methods. In addition to achieving high energy outputs, c-RIME demonstrates higher operational stability, as evidenced by smaller fluctuation values. During the startup test, its Δv^{max} reaches 12.99%, while Δv^{avg} follows a comparable trend, prominently outperforming other algorithms. This indicates c-RIME's ability to maintain operational stability when suffering from uneven solar irradiation. Although c-RIME does not always exhibit the lowest fluctuation metrics as it prioritizes energy capture over absolute stability, its fluctuation levels remain within acceptable ranges, achieving a balance between maximizing energy output and maintaining system stability. While the c-RIME algorithm exhibits superior optimization performance across various scenarios, it introduces a slightly higher computational cost due to the chaotic initialization and multi-phase search structure. This overhead is acceptable for most benchmark cases, though scalability to very large-scale systems may require further optimization. It is also worth noting that current evaluations are conducted in a controlled laboratory environment. In real-world engineering applications, the algorithm may encounter additional challenges such as system uncertainty and

external noise. These aspects will be considered in future work to further validate and adapt the proposed method for practical deployment.

B. Environmental Assessment

The advancement of renewable energy technologies is motivated by the goal of minimizing environmental impact, supporting sustainable growth, and achieving Net Zero objectives. The energy industry, being the primary contributor to carbon emissions, heavily relies on traditional coal- and gas-fired power plants. While carbon capture, utilization, and storage (CCUS) technologies have reduced emissions, their carbon footprint remains far higher than that of renewable energy systems.

Since PV-TEG hybrid systems still lack mature and large-scale commercial applications, comprehensive carbon emission data regarding this type of configuration is currently unavailable. Therefore, this study relies on data from standalone PV systems for a simplified assessment. Since the TEG component contributes only about one-thirtieth of the PV system's total power output, its overall impact is relatively minor. Although the inclusion of TEG affects overall efficiency and emissions, its limited contribution justifies its exclusion from detailed life-cycle assessments. Thus, using standalone PV system data provides a practical and realistic basis for evaluating the carbon reduction potential of the PV-TEG system under the current data and research status. This scheme introduces minimal deviation in the overall assessment, as the TEG's marginal power contribution limits its influence on lifecycle emissions, and the dominant role of the PV component ensures that the primary emission profile is accurately captured.

To conduct the analysis, a comprehensive assessment framework is developed, incorporating carbon emission factors from different electricity generation methods. These include PV power generation, coal-fired, coal-fired with CCUS, gas-fired with CCUS, and general power grid emission factors. Carbon reduction benefits are calculated using [46]:

$$R_{\mathrm{CE}} = E_{\mathrm{gen}} \times E_{\mathrm{FPV}} - E_{\mathrm{gen}} \times E_{\mathrm{Fother}} \tag{29}$$

where R_{CE} means the reduced carbon emissions; E_{gen} represents the energy output; E_{FPV} denotes the PV system carbon emission factor; and E_{Fother} corresponds to the emission factor of other fuel types.

This study uses actual annual output data from a 130 kW PV station in Ningxia, China, to conduct the analysis. The station's power generation curve for 2022 is shown in Fig. 20, with data sampled at 15-min intervals.

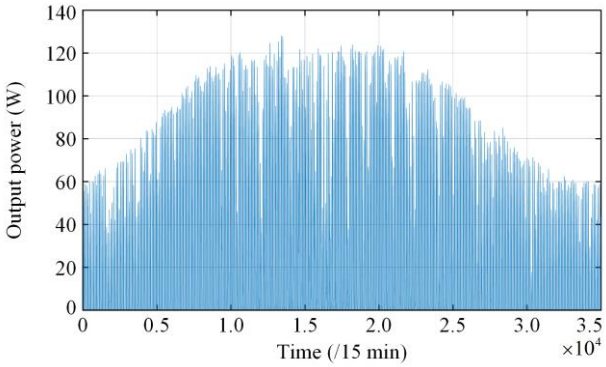

Fig. 20. Power output of a PV station in China with a capacity of 130 kW in 2022.

Technical results indicate that the proposed c-RIME significantly enhances energy output compared to the traditional P&O method. Based on the PV output data, total energy generation is 210 336 kWh and 277 818 kWh using P&O and c-RIME, respectively. Furthermore, the c-RIME algorithm, being model-free and suitable for black-box scenarios, exhibits strong adaptability to the studied system. To further assess the environmental benefits, a life cycle assessment (LCA) is conducted using literature-based carbon emission factors [47]–[50]. Table V provides a detailed comparison of emissions across different electricity generation methods in China, based on the production of 277 818 kWh. Results reveal that the optimized PV technology significantly reduces emissions compared to traditional and modernized fossil fuel systems. Overall, more efficient MPPT techniques ensure higher electricity generation from the same PV area, thereby reducing the carbon intensity of electricity production.

TABLE V
CARBON EMISSION EVALUATION RESULTS

Benchmark	Technology type	CO_2 emission factor (kg CO_2 / kWh)	Total CO_2 emission (kg)
Coal-fired units	Conventional high-pressure coal-fired units	1.063	295 320.917
	Coal with CCUS	0.877	243 646.702
Gas-fired units	Gas with CCUS	0.392	108 904.797
Power grid	Average emissions of China's national power grid	0.570	158 356.465
PV system	PV system with c-RIME MPPT	0.061	16 946.919

VI. CONCLUSIONS

This work develops a c-RIME-based energy optimization strategy for hybrid PV-TEG systems, to enhance energy output and minimize carbon emissions under

varying operational scenarios. The main contributions of this work are outlined as follows.

1) By integrating PV and TEG systems, solar energy is effectively harnessed alongside waste heat reuse. The thermal energy transferred to the TEG modules not only generates electricity but also serves as a passive cooling mechanism for PV modules, thereby improving overall energy efficiency while mitigating performance degradation.

2) The c-RIME based strategy addresses the challenges posed by PSCs, ensuring optimal power generation across diverse conditions. Compared to conventional techniques, it significantly improves both energy yield and operational reliability.

3) The proposed method is validated through four case studies and comprehensive robustness tests, including scenarios using real-world atmospheric data from Hong Kong. These evaluations confirm its effectiveness and reliability under dynamic and diverse environmental conditions.

4) Beyond technical performance, this study evaluates environmental impact using LCA and real-world carbon emission data from various electricity generation methods. The results confirm the carbon reduction potential of the proposed strategy and provide a comprehensive understanding of its environmental impact.

Given the current limitations of this study, future research will focus on three key areas.

1) Optimized system configuration and simplified control: The present system employs two DC-DC converters with separate controllers to ensure reliable control and enhance power output. Although effective, this setup increases cost and complexity. Future research will explore more efficient and cost-effective hybrid PV-TEG configurations, aiming to simplify the control system and reduce associated expenses while maintaining performance.

2) Enhanced carbon reduction analysis: The current carbon reduction analysis adopts a simplified method. Future research will prioritize the collection and evaluation of real-world datasets from real pilots, enabling more accurate carbon footprint assessments and promoting further development of sustainable energy applications.

3) Future work will also include experimental validation and real-time implementation of the proposed c-RIME strategy. A prototype PV-TEG system with embedded MPPT control will be developed to assess the algorithm's practical performance, scalability, and energy conversion efficiency under actual operating conditions.

ACKNOWLEDGMENT

Not applicable.

AUTHORS' CONTRIBUTIONS

Jingbo Wang: conceptualization, writing-original draft, formal analysis, and software. Jianfeng Wen: formal analysis, validation, and data curation. Shaocong Wu: software, investigation, and visualization. Bo Yang: resources and funding acquisition. Pingliang Zeng: writing-reviewing & editing and resources. Lin Jiang: writing-reviewing & editing and supervision. All authors read and approved the final manuscript.

FUNDING

This work is supported by the National Natural Science Foundation of China (No. 62263014) and Yunnan Provincial Basic Research Project (No. 202401AT070344 and No. 202301AT070443).

AVAILABILITY OF DATA AND MATERIALS

Please contact the corresponding author for data material request.

DECLARATIONS

Competing interests: The authors declare that they have no known competing financial interests or personal relationships that could have appeared to influence the work reported in this article.

AUTHORS' INFORMATION

Jingbo Wang received the B.S. and M.S. degrees in electrical engineering from Kunming University of Science and Technology, Kunming, China, in 2019 and 2022, respectively. He is currently pursuing his Ph.D. degree at the Department of Electrical Engineering & Electronics, University of Liverpool, Liverpool, UK. His main research interests include renewable energy system optimization and control, and power sector decarbonization.

Jianfeng Wen is the research assistant at the University of Liverpool. He received the B.S. and M.Eng. degrees in electrical engineering from Huazhong University of Science and Technology, Wuhan, China, in 2018 and 2020, respectively. Then he obtained the Ph.D. degree in electrical engineering from the University of Liverpool in 2024, Liverpool, UK. His research interests include control and energy management of micro-grid systems, and electrified transportation optimization.

Shaocong Wu received the B.S. and M.S. degrees in electrical engineering from Kunming University of Science and Technology, Kunming, China, where he is currently pursuing the Ph.D. degree at the School of Electrical Engineering, Shandong University. His research interests include renewable energy systems and smart grid operation.

Bo Yang received the B.S. and M.S. degrees in electrical engineering from South China University of Technology, Guangzhou, China, in 2010 and 2011, respectively, and the Ph.D. degree from the Department of Electrical Engineering, University of Liverpool, Liverpool, UK, in 2015. Since 2016, he has been working at Kunming University of Science and Technology. In 2020, he was appointed as a professor at Kunming University of Science and Technology, and further accoladed as a doctoral supervisor in 2022. He is currently with the Faculty of Electric Engineering, Kunming University of Science and Technology, Kunming, China. He specializes in the applications of artificial intelligence in the optimization and control of renewable energy power generation systems.

Pingliang Zeng received the B.S. and Ph.D. degrees in Electrical Engineering from Huazhong University of Science and Technology, China, and Strathclyde University, UK, in 1984 and 1990, respectively. He is currently a professor in Hangzhou Dianzi University, Hangzhou, China. His current research interests are power system planning, integration of energy storage in low carbon electricity systems.

Lin Jiang graduated with the B.Eng. and M.Sc. degree from Huazhong University of Science and Technology, Wuhan, China, and the Ph.D. degree from the University of Liverpool, UK, all in electrical engineering in 1992 and 1996 and 2001, respectively. His research interests include nonlinear adaptive control, power system automation, and smart grid.

REFERENCES

[1] X. Wu, W. Yang, and N. Zhang *et al*., "A distributed computing algorithm for electricity carbon emission flow and carbon emission intensity," *Protection and Control of Modern Power Systems*, vol. 9, no. 2, pp. 138-146, Mar. 2024.

[2] F. Dong, Y. Li, and Y. Gao *et al*., "Energy transition and carbon neutrality: exploring the non-linear impact of renewable energy development on carbon emission efficiency in developed countries," *Resources, Conservation and Recycling*, vol. 177, Feb. 2022.

[3] S. Fan, Y. Wang, and S. Cao *et al*., "A novel method for analyzing the effect of dust accumulation on energy efficiency loss in photovoltaic (PV) system," *Energy*, vol. 234, Nov. 2021.

[4] E. H. Amalu and O. A. Fabunmi, "Thermal control of crystalline silicon photovoltaic (c-Si PV) module using Docosane phase change material (PCM) for improved performance," *Solar Energy*, vol. 234, pp. 203-221, Mar. 2022.

[5] Z. Yin, T. Zhang, and J. Cai *et al*., "Investigation on the operating characteristics of a directly-attached light crystalline silicon PV roof," *Solar Energy*, vol. 262, Sep. 2023.

[6] E. Jamali, M. H. Nobakhti, and B. M. Ziapour *et al*., "Performance analysis of a novel model of photovoltaic PV-TEGs system enhanced with flat plate mirror reflectors," *Energy Conversion and Management*, vol. 279, Mar. 2023.

[7] O. F. Eikeland, C. C. Kelsall, and K. Buznitsky *et al*., "Power availability of PV plus thermal batteries in real-world electric power grids," *Applied Energy*, vol. 348, Mar. 2023.

[8] Y. Gao, D. Wu, and Z. Dai *et al*., "A passive evaporative cooling strategy to enhance the electricity production of hybrid PV-STEG system," *Applied Energy*, vol. 349, Nov. 2023.

[9] D. De Luca, P. Strazzullo, and E. Di Gennaro *et al*., "High vacuum flat plate photovoltaic-thermal (HV PV-T) collectors: efficiency analysis," *Applied Energy*, vol. 352, Dec. 2023.

[10] B. Yang, C. Zeng, and D. Li *et al*., "Improved immune genetic algorithm-based TEG system reconfiguration under non-uniform temperature distribution," *Applied Energy*, vol. 325, Nov. 2022.

[11] K. Tyagi, B. Gahtori, and S. Kumar *et al*., "Advances in solar thermoelectric and photovoltaic-thermoelectric hybrid systems for power generation," *Solar Energy*, vol. 254, pp. 195-212, Apr. 2023.

[12] M. A. Qasim, V. I. Velkin, and S. E. Shcheklein, "Experimental study on hybridization of a PV-TEG system for electrical performance enhancement using heat exchangers, energy, exergy and economic levelized cost of energy (LCOE) analysis," *Clean Energy*, vol. 7, no. 4, pp. 808-823, Aug. 2023.

[13] C. Babu and P. Ponnambalam, "The role of thermoelectric generators in the hybrid PV/T systems: a review," *Energy Conversion and Management*, vol. 151, pp. 368-385, Nov. 2017.

[14] E. Skoplaki and J. A. Palyvos, "Operating temperature of photovoltaic modules: a survey of pertinent correlations," *Renewable Energy*, vol. 34, no. 1, pp. 23-29, Jan. 2009.

[15] B. Yang, R. Xie, and S. Wu, *et al.*, "Hybrid PV-TEG system maximum power point tracking based on an exponential distribution optimizer," *Power System Protection and Control*, vol. 52, no. 16, pp. 12-25, Aug. 2024. (in Chinese)

[16] S. Manna, A. K. Akella, and D. K. Singh, "Novel Lyapunov-based rapid and ripple-free MPPT using a robust model reference adaptive controller for solar PV system," *Protection and Control of Modern Power Systems*, vol. 8, no. 1, pp. 1-25, Jan. 2023.

[17] B. Yang, Y. Li, and J. Huang *et al*., "Modular reconfiguration of hybrid PV-TEG systems via artificial rabbit algorithm: modelling, design and HIL validation," *Applied Energy*, vol. 351, Dec. 2023.

[18] X. Zhang, T. Tan, and B. Yang *et al*., "Greedy search-based data-driven algorithm of centralized thermoelectric generation system under non-uniform temperature distribution," *Applied Energy*, vol. 260, Feb. 2020.

[19] S. Singh, S. Saini, and S. K. Gupta *et al*., "Solar-PV inverter for the overall stability of power systems with intelligent MPPT control of DC-link capacitor voltage," *Protection and Control of Modern Power Systems*, vol. 8, no. 1, pp. 1-20, Jan. 2023.

[20] B. Yang, R. Xie, and J. Duan *et al*., "State-of-the-art review of MPPT techniques for hybrid PV-TEG systems: modeling, methodologies, and perspectives," *Global Energy Interconnection*, vol. 6, no. 5, pp. 567-591, Oct. 2023.

[21] S. Mohanty, B. Subudhi, and P. K. Ray, "A grey wolf-assisted perturb & observe MPPT algorithm for a PV system," *IEEE Transactions on Energy Conversion*, vol. 32, no. 1, pp. 340-347, Mar. 2017.

[22] S. Motahhir, A. Chalh, and A. El Ghzizal *et al*., "Development of a low-cost PV system using an improved INC algorithm and a PV panel Proteus model," *Journal of Cleaner Production*, vol. 204, pp. 355-365, Dec. 2018.

[23] A. Refaat, Q. A. Ali, and M. M. Elsakka *et al*., "Extraction of maximum power from PV system based on horse herd optimization MPPT technique under various weather conditions," *Renewable Energy*, vol. 220, Jan. 2024.

[24] X. Zhang, B. Yang, and T. Yu *et al*., "Dynamic surrogate model-based optimization for MPPT of centralized thermoelectric generation systems under heterogeneous temperature difference," *IEEE Transactions on Energy Conversion*, vol. 35, no. 2, pp. 966-976, Jun. 2020.

[25] J. A. Salim, B. M. Albaker, and M. S. Alwan *et al*., "Hybrid MPPT approach using cuckoo search and grey wolf optimizer for PV systems under variant operating conditions," *Global Energy Interconnection*, vol. 5, no. 6, pp. 627-644, Dec. 2022.

[26] M. Sarvi and A. Azadian, "A comprehensive review and classified comparison of MPPT algorithms in PV systems," *Energy Systems*, vol. 13, no. 2, pp. 281-320, May 2022.

[27] N. M. Khan, M. Mansoor, and A. F. Mirza *et al*., "Energy harvesting and stability analysis of centralized TEG system under non-uniform temperature distribution," *Sustainable Energy Technologies and Assessments*, vol. 52, Aug. 2022.

[28] M. K. Khan, M. H. Zafar, and M. Mansoor *et al*., "Green energy extraction for sustainable development: a novel MPPT technique for hybrid PV-TEG system," *Sustainable Energy Technologies and Assessments*, vol. 53, Aug. 2022.

[29] A. F. Mirza, M. Mansoor, and K. Zerbakht *et al*., "High-efficiency hybrid PV-TEG system with intelligent control to harvest maximum energy under various non-static operating conditions," *Journal of Cleaner Production*, vol. 320, Oct. 2021.

[30] B. Yang, S. Wu, and J. Huang *et al*., "Salp swarm optimization algorithm-based MPPT design for PV-TEG hybrid system under partial shading conditions," *Energy Conversion and Management*, vol. 292, Sep. 2023.

[31] V. Verma, A. Kane, and B. Singh, "Complementary performance enhancement of PV energy system through thermoelectric generation," *Renewable and Sustainable Energy Reviews*, vol. 58, pp. 1017-1026, May 2016.

[32] U. A. Saleh, M. A. Johar, and S. A. B. Jumaat *et al*., "Evaluation of a PV-TEG hybrid system configuration for an improved energy output: a review," *International Journal of Renewable Energy Development*, vol. 10, no. 2, pp. 385-400, May 2021.

[33] M. A. El-Dabah, R. A. El-Sehiemy, and H. M. Hasanien *et al*., "Photovoltaic model parameters identification using northern goshawk optimization algorithm," *Energy*, vol. 262, Jan. 2023.

[34] X. Han, T. Wang, and X. Wei, *et al.*, "Ultrashort-term photovoltaic output forecasting considering spatiotemporal correlation between arrays," *Power System Protection and Control*, vol. 52, no. 14, pp. 82-94, Jul. 2024. (in Chinese)

[35] O. Bingöl and B. Özkaya, "Analysis and comparison of different PV array configurations under partial shading conditions," *Solar Energy*, vol. 160, pp. 336-343, Jan. 2018.

[36] X. Fang, Q. Yang, and W. Yan, "Power generation maximization of distributed photovoltaic systems using dynamic topology reconfiguration," *Protection and Control of Modern Power Systems*, vol. 7, no. 3, pp. 1-15, Jul. 2022.

[37] Y. Liu, Y. H. Chiu, and J. Huang *et al*., "A novel maximum power point tracker for thermoelectric generation system," *Renewable Energy*, vol. 97, pp. 306-318, Nov. 2016.

[38] H. Su, D. Zhao, and A. A. Heidari *et al*., "RIME: a physics-based optimization," *Neurocomputing*, vol. 532, pp. 183-214, May 2023.

[39] R. S. Vieira and R. A. Mosna, "Homoclinic chaos in the Hamiltonian dynamics of extended test bodies," *Chaos, Solitons & Fractals*, vol. 163, Oct. 2022.

[40] E. Varol Altay and B. Alatas, "Bird swarm algorithms with chaotic mapping," *Artificial Intelligence Review*, vol. 53, no. 2, pp. 1373-1414, Feb. 2020.

[41] G. A. Raiker and U. Loganathan, "Current control of boost converter for PV interface with momentum-based perturb and observe MPPT," *IEEE Transactions on Industry Applications*, vol. 57, no. 4, pp. 4071-4079, Aug. 2021.

[42] L. Abualigah, M. Abd Elaziz, and P. Sumari *et al*., "Reptile search algorithm (RSA): a nature-inspired meta-heuristic optimizer," *Expert Systems with Applications*, vol. 191, Apr. 2022.

[43] S. Mirjalili, S. M. Mirjalili, and A. Hatamlou, "Multi-verse optimizer: a nature-inspired algorithm for global optimization," *Neural Computing and Applications*, vol. 27, pp. 495-513, Feb. 2016.

[44] S. Mirjalili, "Moth-flame optimization algorithm: a novel nature-inspired heuristic paradigm," *Knowledge-Based Systems*, vol. 89, pp. 228-247, Nov. 2015.

[45] S. Mirjalili, "SCA: a sine cosine algorithm for solving optimization problems," *Knowledge-Based Systems*, vol. 96, pp. 120-133, Mar. 2016.

[46] N. K. Singh, A. Goswami, and P. K. Sadhu, "Energy economics and environmental assessment of hybrid hydel-floating solar photovoltaic systems for cost-effective low-carbon clean energy generation," *Clean Technologies and Environmental Policy*, vol. 25, no. 4, pp. 1339-1360, May 2023.

[47] M. An and X. Sun, "Carbon footprints of solar panels in China provinces based on different production and waste treatment scenarios," *Journal of Cleaner Production*, vol. 435, Jan. 2024.

[48] X. Guo, Y. Dong, and D. Ren, "CO_2 emission reduction effect of photovoltaic industry through 2060 in China," *Energy*, vol. 269, Apr. 2023.

[49] International Energy Agency (IEA), "*Enhancing China's ETS for Carbon Neutrality: Focus on Power Sector*," IEA, Paris. [Online]. Available: https://www.iea.org/reports/enhancing-chinas-ets-for-carbon-neutrality-focus-on-power-sector, Licence: CC BY 4.0

[50] S. Zhang, J. Zhang, and F. Bu *et al*., "A practical method for calculating indirect carbon emissions of electricity users in large power grid," in *the Proceedings of 2023 International Conference on Wireless Power Transfer* (ICWPT 2023), Singapore, Singapore, Mar. 2024, pp. 45-55.